Intermittent structures and quasi-stationary equilibrium in a simple magnetized torus in open field line configuration

Journal of Physics Communications

PAPER

Intermittent structures and quasi-stationary equilibrium in a simple magnetized torus in open field line configuration

Prince Alex, Ruggero Barni, Hector Eduardo Roman and Claudia Riccardi

Dipartimento di Fisica G.Occhialini, Università degli Studi di Milano-Bicocca, Piazza della Scienza 3, Milano 20126, Italy

E-mail: princealexanderm@gmail.com

Keywords: edge physics, turbulence and transport, magnetic confinement, toroidal plasma

OPEN ACCESS

RECEIVED
18 November 2021

REVISED
15 January 2022

ACCEPTED FOR PUBLICATION
19 January 2022

PUBLISHED
31 January 2022

Abstract

A steady regime dominated by intermittent blob and hole structures is identified in the plasma state of a simple magnetized torus by achieving a quasi-stationary equilibrium using an open magnetic field line configuration. The open helical field line configuration is characterized by a connection length, $L_c = 2a\left(\frac{B_\varphi}{B_z}\right) \gtrsim 1750$ cm, and pitch ratio, $r_B = \frac{B_z}{B_\varphi} \lesssim 0.01$. This is realized by superposing a vertical magnetic fied, B_z, to the toroidal field, B_φ, and the regime is achieved for $B_z \leqslant 0.4$ mT. The combined effect of plasma rotation, arising from a substantial radial electric field, together with an open field line, results in vertically elongated plasma profile and an asymmetric sheared poloidal flow. The analysis shows the existence of density fluctuations exhibiting universal statistical properties, dominated by non-Gaussian blob events in the edge region and holes in the core plasma, separated by a region ascribed as blob birth zone corresponding to a velocity shear layer. Two-dimensional conditional averaging analyses of fluctuations indicate that blobs form in the sheared layer, when the leading edge of an elongated coherent structure breaks off by differential stretching exerted by the background fluctuating field. Convection of this isolated blob out of the contour corresponding to the maximum radial electric field in the low field side, leads to its ejection while holes move along the same contour driven back into the main plasma. The corresponding potential structure shows counter-rotating $\boldsymbol{E} \times \boldsymbol{B}$ velocity field within oppositely charged structures, where the embedded electric field is consistent with the observed structure propagation. A comparison with cross-correlation analysis yields a similar conclusion except for a slight overestimation of the structure size and lifetime.

1. Introduction

It has long been identified that turbulent fluctuations have a bursty intermittent behaviour, generally known as intermittent plasma objects or blob filaments, being responsible for nearly 50% of the particle transport in the edge scrape-off layer (SOL) transport of fusion devices [1–7]. They enhance the plasma interaction with the surrounding wall material boundaries and lead to serious wall erosion, impurity and recycling problems, which also in future devices such as ITER if left unaddressed [8, 9]. Since turbulence in general has a spatio-temporal nature, experiments in fusion devices often suffer a setback arising from diagnostics access and statistical uncertainities, restricting the reconstruction of the spatio-temporal evolution of turbulent structures only to a limited portion of the plasma cross-section. Furthermore, recent computational studies have shown that evaluating the exact structure shapes, and the associated trajectories, could be laborious due to the large number of factors that need to be taken into account such as, magnetic geometry, collisionality, 3D effects, kinetic effects in addition to background instability and sheared flow [10–12]. To complement this, one could observe that turbulence studies in numerical simulations and basic plasma experiments, have greatly aided in overcoming these difficulties up to some extent with the adoption of more simplified frameworks [13–21]. Basic low-temperature plasma devices, optimized for turbulence studies, enable one to perform diagnostics with sufficient spatial and temporal resolution to extract a wealth of information where equilibrium conditions can be typically

achieved in a highly controllable plasma under steady-state operation. In this work, we study the characteristics of intermittent structures in a simple magnetized torus (SMT). By collecting data having suitable spatial and temporal resolution, in a low-temperature toroidal plasma device with an open field-line magnetic configuration, we identified two basic structures. Here we discuss a plasma regime dominated by continuous formation and transport into the edge of blobs and holes after achieving a quasi-stationary equilibrium.

Intermittent plasma objects are magnetic field-aligned plasma structures having densities significantly higher (blob) or lower (hole) than the surrounding background plasma and are localized in the direction perpendicular to the field [22]. Though extensive literature is available on such structures from both fusion and basic devices, identifying their location, formation, generation mechanism, and propagation under different plasma backgrounds are still considered to be very challenging. Theory and simulation predict their generation is associated with the nonlinear saturation of the background magnetohydrodynamic (MHD) instability, and their motion is propelled by the $\boldsymbol{E} \times \boldsymbol{B}$ drift due to the electric field $\boldsymbol{E}$ arising from the curvature and $\nabla|\boldsymbol{B}|$ effects in toroidal devices [22]. Reported studies associate an interchange instability as one of the dominant blob generation mechanisms in toroidal devices, while quasi-coherent drift wave and drift wave turbulence playing the role in linear devices and stellarators respectively [5, 16, 23]. At the same time, gyro-fluid simulations performed in the vicinity of the separatrix indicate that blob formation is not bound to one particular location or instability [10]. A recently proposed universal mechanism suggests that their generation is different in the presence of poloidal velocity shear or of a radial velocity shear in the absence of the former [24].

The SMT devices have attracted a great deal of interest in the past as a testbed to explore the detection and study the transport of such structures, due to its geometrical similarities with fusion devices such as curvature and gradient in magnetic field [25–39]. But due to the lack of MHD equilibrium in the closed field line configuration, structures detected using 2D probe arrays were mostly mode-like, large-scale coherent structures, rather than intermittent ones [40, 41]. By convention, intermittency requires density fluctuations to be dominated by spiky events with intensity exceeding a threshold value of a standard deviation. This implies a non-Gaussian positively (negatively) skewed probability distribution function (PDF) as one of the necessary conditions for the detection of blob (hole) in the single point Langmuir probe measurement [22], or a steep leading edge and gentle trailing wake in the conditionally averaged waveform as the signature of blob ejected from the unstable main plasma region into the SOL [13].

Recently, an unambiguous identification of intermittent structures in SMT device TORPEX with ECR plasma source has been demonstrated under open field line Helimak configuration [42–44], by achieving quasi-stationary equilibrium in a plasma dictated by radial shear [38, 45]. In a regime dominated by a parallel loss, given by $N \leqslant 7$ or $B_z \geqslant 1$ mT, intermittent blob structures are observed to form from a radially elongated structure at the region where the logarithmic pressure gradient is maximum, where N is the maximum number of toroidal turns made by the field lines inside the device [46, 47]. In the present study, investigations are carried out to explore the existence of such structures and understand its dynamics in the SMT device THORELLO, characterized by a thermionic discharge plasma [34]. Unlike the previous device, the presence of substantial radial electric field arising from the negative biasing of plasma source, together with open field line configuration, results in a poloidally asymmetric sheared rotating plasma. Specifically, the study focuses on the dynamics in a background plasma defined as $\nu'_z > \nu'_a$, where ν'_z is the poloidal velocity shear and ν'_a is the radial velocity shear. We identified a suitable regime dominated by parallel loss for $B_z \leqslant 0.4$ mT, again corresponding to a $N \geqslant 7$ condition. Since SOL transport, controlled by intermittent structures, is known to define the width of the edge pedestals of density and temperature, and blob interaction with the sheared flow in scenarios such as the L-H transition is still a topic of active discussion in fusion devices, a better understanding of the intermittent convective transport under varying background plasma conditions is necessary to improve the understanding of intermittent turbulent transport in more general circumstances. Radial variation of higher-order moments of PDF is found to be similar to that observed in SOL of fusion devices. Spatial identification of both blob and hole structures, their formation mechanism, role of shear layer, conditions for ejection, the role of potential structures in its propagation are being investigated using time-averaged measurements, conditional averaging techniques and cross-correlation measurements.

The remaining part of the paper is organized as follows. A brief description of the experimental setup, plasma production and diagnostics are described in section 2. Open field line configuration presented in this study and resulting quasi-stationary equilibrium scenario is discussed in section 3. A description of the time-averaged background profiles is given in section 4. Basic statistical properties of the observed fluctuations exhibiting universal statistical properties and identification of intermittent structures are described in section 5. Spatio-temporal evolution of density (blobs and holes) and potential structures and mechanism of blob formation are given in section 6. A correlation analysis performed to verify the conditional averaging results is also provided in this section. Finally, the results are summarized in section 7.

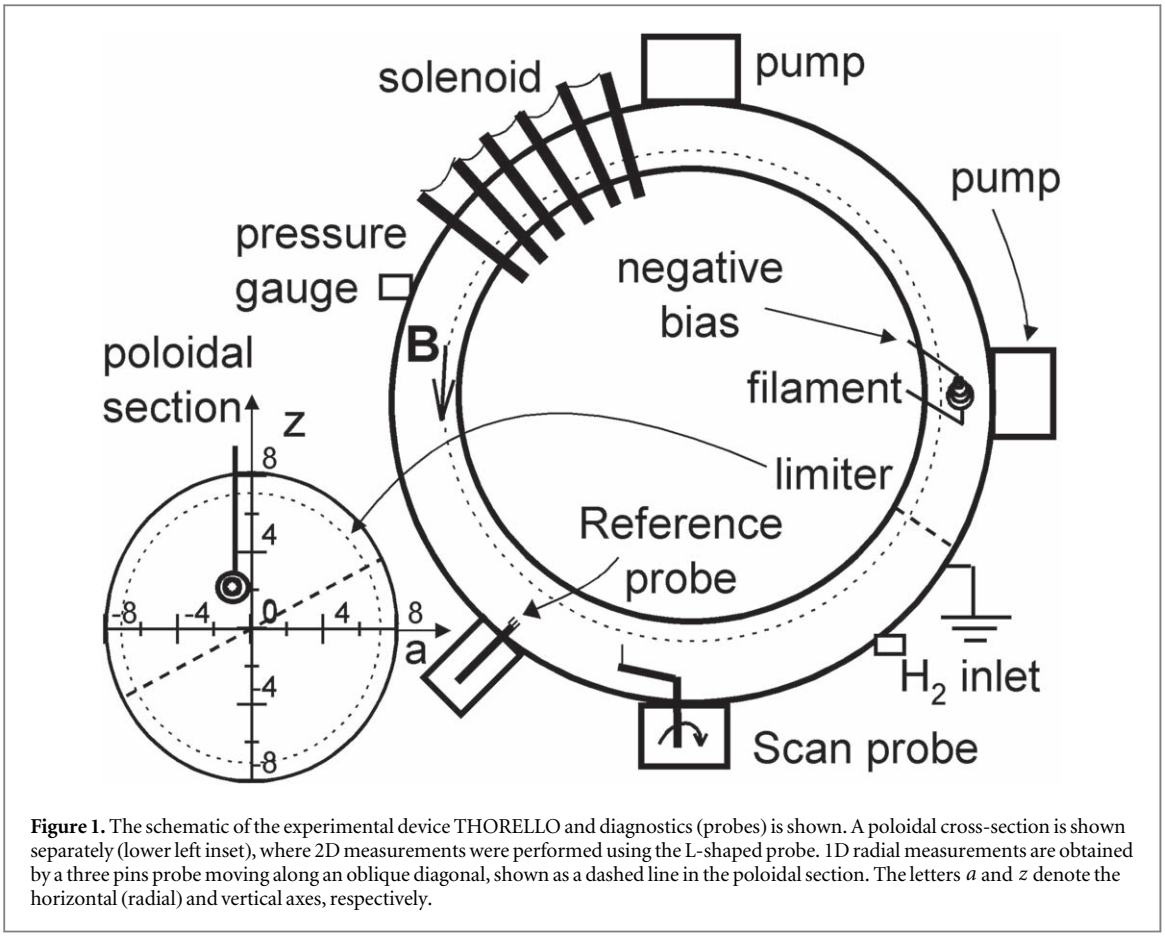

Figure 1. The schematic of the experimental device THORELLO and diagnostics (probes) is shown. A poloidal cross-section is shown separately (lower left inset), where 2D measurements were performed using the L-shaped probe. 1D radial measurements are obtained by a three pins probe moving along an oblique diagonal, shown as a dashed line in the poloidal section. The letters a and z denote the horizontal (radial) and vertical axes, respectively.

2. Experimental setup and diagnostics

The schematic of the experimental setup THORELLO is shown in figure 1. It is a SMT device with a major radius of $R = 400$ mm and a minor radius of $a = 87.5$ mm, and the toroidal geometry of the vacuum vessel is realized by combining four toroidal sectors. A set of 56 evenly spaced toroidal field coils, is used for the generation of maximum toroidal field (B_φ) of up to 0.2 T. Plasma is produced using thermionic discharge by a hot tungsten filament emission. The plasma source consists of a 13.5 turns conical spiral of tungsten braided wire aligned to the magnetic field. The spiral has an oval extension of 1.9 cm by 2.6 cm in the plane perpendicular to the magnetic field, placed inside the torus approximately at $(a, z) = (-10,30)$ mm, where a and z are the radial and vertical plane coordinates. Discharge in the system is ignited by biasing the filament, acting as cathode, negatively at a potential of -90 V with respect to the walls and to the grounded limiter (a 150 mm diameter hollow disk). Two additional circular coils, each having a radius of 800 mm in Helmholtz arrangement, are fixed in a plane parallel to the equatorial plane with a vertical separation of 800 mm for the purpose of creating a vertical field (B_Z). Hydrogen gas, injected into the chamber up to a fill pressure $P \simeq 4 \times 10^{-4}$ mbar.

The diagnostics for the time-resolved measurements discussed in this work have been carried out using electrostatic Langmuir probes. One-dimensional measurements are performed using a radially movable 3 pins probe, scanning a diameter inclined 30° in the poloidal section. The 2D measurements of the complete poloidal section are obtained using a L-shaped probe, moving radially and rotating about its axis [48]. Both probes carry a 5 mm long and 0.3 mm diameter tungsten wire used as a sensing tip. Langmuir characteristics measurements are acquired by summing up nearly 64 probe current curves by sweeping the probe potential of 100 V in 0.1 s, which is used for the estimation of plasma parameters such as plasma density (n_e), electron temperature (T_e), floating potential (V_f) and plasma potential (V_P). For the fluctuation analysis, time series of density fluctuations are measured with probe biased at -90 V so as to collect the ion saturation current signal. Floating potential fluctuations are recorded with a probe terminated at high impedance. Generally, time series are digitized at a sampling rate of 2 MHz with a data length of 2.05 10^6 points by a digital scope. To obtain information about the spatio-temporal evolution of fluctuating structures, we performed a conditional sampling analysis [49] (see section 6). In these measurements, the oblique probe fixed at $(a, z) = (25,15)$ mm is used as the reference probe to trigger the events of interest, while the L-shaped probe scans the whole poloidal locations with a resolution of 10 mm.

3. Open field line configuration and quasi-stationary equilibrium

Unlike tokamak, plasma confined by closed field lines in SMTs are not in MHD equilibrium due to the lack of rotational transform. The vertical electric field, arising from the charge polarization due to curvature and gradient in magnetic field, drifts the entire plasma radially outwards, reducing confinement. The presence of $\boldsymbol{E_r} \times \boldsymbol{B_\varphi}$ plasma rotation has been suggested as a mechanism to short-circuit charge accumulation via transport from top to bottom and vice versa, allowing to obtain a steady plasma state in purely SMT configuration. Recently, it was demonstrated that SMTs in Helimak configuration limits the build-up of the vertical electric field effectively, allowing to establish a quasi-stationary equilibrium [45]. Here, the conventional closed field lines are opened up by the application of a vertical magnetic field, superimposed to the toroidal magnetic field. Field lines within the device, which now have a pitch angle, intersect the limiter or the walls at both the top and the bottom of the vessel thus drawing a parallel current. The plasma is then confined by the current which can flow through a closed loop, via a conducting limiter or vessel, for significantly longer time than the purely toroidal field line leading the profiles to be vertically elongated. The magnetic configuration is controlled by the resultant magnitude of the field, $B = (B_\varphi^2 + B_Z^2)^{1/2}$ and by the open helical field line maximal length $L_c = 2a(\frac{B_\varphi}{B_Z})$, the pitch ratio $r_B = \frac{|B_Z|}{B}$. Alternatively, it can be expressed through the pitch $\Delta = 2\pi R(\frac{B_Z}{B_\varphi})$, the distance between points of two nearby toroidal field lines in the same poloidal plane or $N = 2a/\Delta$, the maximum number of toroidal turns of the magnetic field lines within the vessel.

In the present study, we have explored the intermittent structure dynamics in Helimak configuration for a vertical field of magnitude $B_Z = 0.3$mT, superposed to a toroidal field $B_\varphi = 40$ mT, where the field line is characterized by $L_c = 2333$ cm, $r_B \simeq 7.5 \times 10^{-3}$, $\Delta \simeq 1.88$ cm and $N = 9$. For the sake of simplicity, L_c is assumed to be constant and estimated at the poloidal center since it is known that $B_\varphi \propto 1/\mathrm{R}$.This selection of the vertical field is based on the following information inferred while varying B_Z from minimum of zero to the maximum possible value. By increasing B_Z from zero, a steady increase in the magnitude of plasma parameters is observed till either $B_Z = 0.4$ mT or $N = 7$ ($L_c = 1750$cm and $r_B = 0.01$) is reached. Above this value, the magnitude of the parameters drops abruptly, as well as a significant change in topology of the plasma profile is observed. For example, for any value of the applied magnetic field, in the range $0 \leqslant B_z \leqslant 0.4$ mT, the 2D profile of plasma potential is characterized by a typical parabolic well geometry, with values increasing towards the limiter from its minimum, while the shape of the potential well changes from parabolic to canyon-shaped, aligned in the z-direction for stronger vertical fields. It is identified that below 0.4 mT, the plasma dynamics is dominated by a cross-field perpendicular loss and above it is governed by a direct parallel loss. The vertical field magnitude, $B_Z = 0.4$ mT, is the threshold value at which both losses are comparable. The observations, in agreement with three-dimensional global fluid simulations, that above and below the threshold, the background instabilities are identified as: Resistive interchange with $k_{||} \neq 0$ and ideal interchange with $k_{||} = 0$, respectively [50]. The present study is performed in the region $0 \leqslant B_z \leqslant 0.4$ mT in order to explore the intermittent dynamics in the perpendicular loss-dominated regime, while the blob dynamics in the other regime ($N < 7$) has been explored earlier in other devices [23]. Early studies in other thermionic discharges showed that when the vertical field B_Z is increased above a threshold value fluctuations levels were drastically reduced [28, 51, 52]. The effect of variation in the vertical field on plasma profile, turbulent dynamics, shear flow, parallel flow, spectral and statistical properties, blob transport, and instabilities will be discussed in the forthcoming publications.

4. Time averaged plasma profiles from Langmuir probe analysis

Two-dimensional time-averaged background plasma profiles obtained in the poloidal cross-section are shown in figure 2. Plasma parameters were extracted by fitting the Langmuir characteristics using electron current to estimate the density and the maximum of the slope position to estimate the plasma potential. The grid locations at which the measurements are carried out is shown in figure 2(a) (black circles). As it is apparent, the density profile, n_e (figure 2(a)) is asymmetric and peaks near the center, having the shape of a cone in the cross-section. The measured density profiles show a slope towards the edges, with values in the range $n_e \simeq 1 \times 10^{16}\mathrm{m}^{-3}$ to $n_e \simeq 2 \times 10^{17}\mathrm{m}^{-3}$. It should be noted that estimations of parameters in the vicinity of the filament shadow, *i.e.* around $a = -10$ mm, are affected by the current deformation by high energy primary electrons. The top-left and top-right regions of the profile are characterized by a very low-density feeble plasma. On the other hand, the electron temperature, T_e (figure 2(b)) shows a localized peak at (−5,15) mm, slightly lower respect to the filament shadow, with its value varying in the range (1–9) eV towards the center. Figure 2(h) shows the floating potential profile where a similarly localized potential well reaching a minimum value of −60 V is observed approximately at the same location. The plasma potential shows a more extended shape. The minimum of the plasma potential, V_p, is observed at the center of the lower half of the poloidal cross-section. Figures 2(d)–(f) show the surface plots of n_e, T_e and V_P, respectively for an alternative view. The observed values of V_P varies from

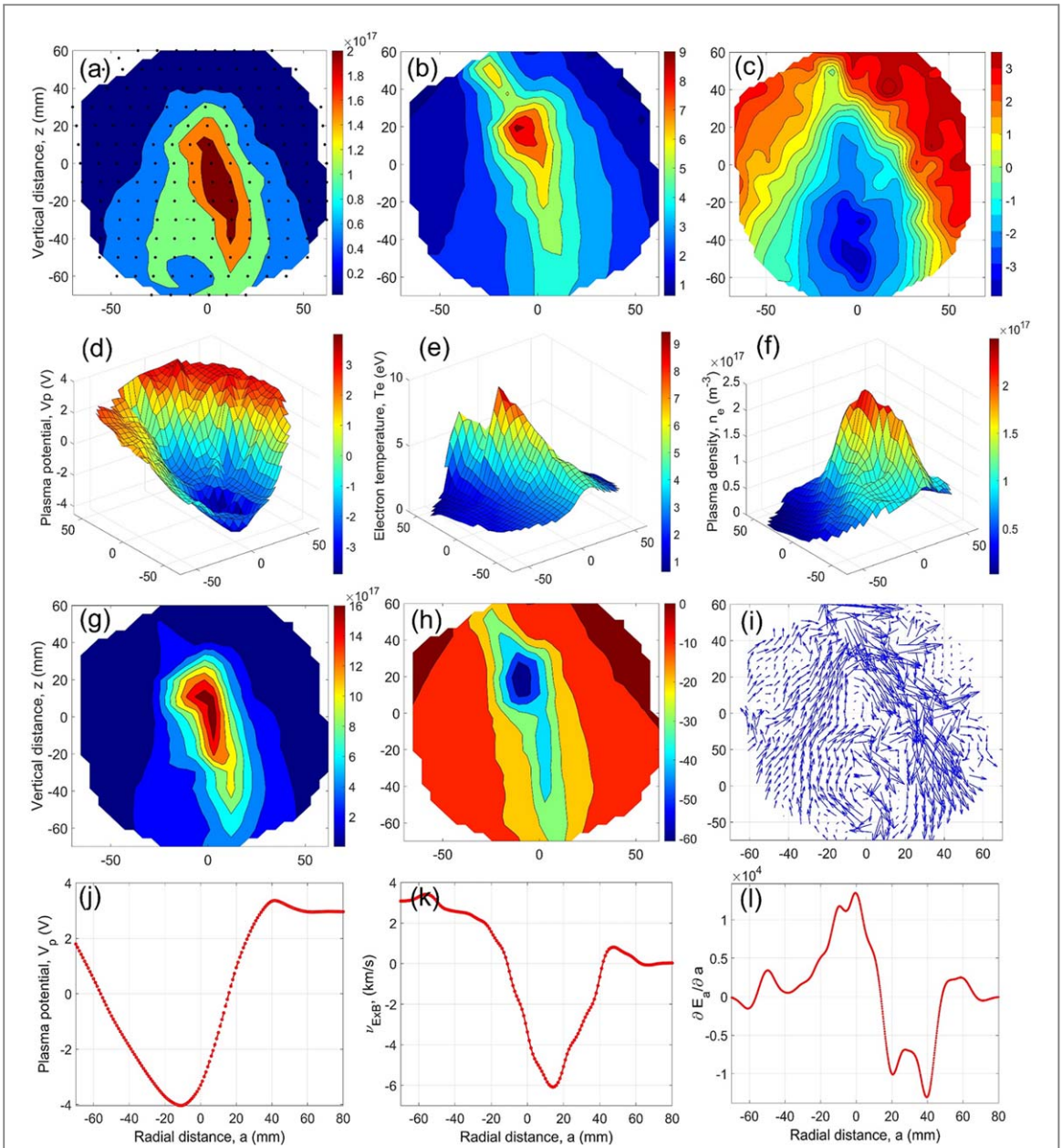

Figure 2. Two dimensional profiles of plasma parameters obtained in the poloidal cross-section are shown. **First row** (a)–(c): Density (n_e), electron temperature (T_e) and plasma potential (V_P). **Second row** (d)–(f): Values corresponding to that of the surface plots. **Third row** (g-i): Plasma pressure, P_e, and floating potential, V_f, and 2D $\boldsymbol{E} \times \boldsymbol{B}$ velocity field. **Fourth row** (j)–(l): 1D plasma potential, 1D $\nu_{E\times B}$ and electric field shear, $\partial E/\partial x$ measured diagonally using oblique probe.

-4 V, at the bottom of the potential well, to $+4$ V at the edges, creating a gradient in V_P and resulting in an inhomogeneous electric field E_r. This produces an overall $\boldsymbol{E} \times \boldsymbol{B}$ drift velocity field which rotates the plasma asymmetrically in the clockwise direction (figure 2(i)). The electron pressure, P_e, is also vertically elongated with a slope towards both sides as in the case of electron temperature (figure 2(g)). The vertically elongated nature of the plasma profiles is attributed to the helical field lines, and is a key signature of a quasi-stationary equilibrium.

Figures 2(j)–(l) show, respectively, 1D plasma potential, $\boldsymbol{E} \times \boldsymbol{B}$ velocity derived from V_P, and electric field shear $\partial E/\partial x$ measured along an inclined line using the oblique probe described in figure 1. The shape broadly agrees with the two dimensional field and it shows a mildly asymmetric potential well centered near the center. It can be observed that the $\boldsymbol{E} \times \boldsymbol{B}$ velocity peaks in the low field side (LFS) at $x = 15$ mm (x being the radial coordinate) given by 6 km s^{-1} downwards, and at the point $x \simeq -5$ mm, it changes sign representing the location of the shear layer (figure 2(l)), *i.e.,* the region where poloidal velocity shear is maximum. While comparing these observations with 2D $\boldsymbol{E} \times \boldsymbol{B}$ flow field shown in figure 2(i), we can see that the shear layer and region of maximum electric field form a poloidally elongated region in the LFS, with the shear layer approximately 20 mm inside. To better characterize the flow regime, we have calculated the radially and

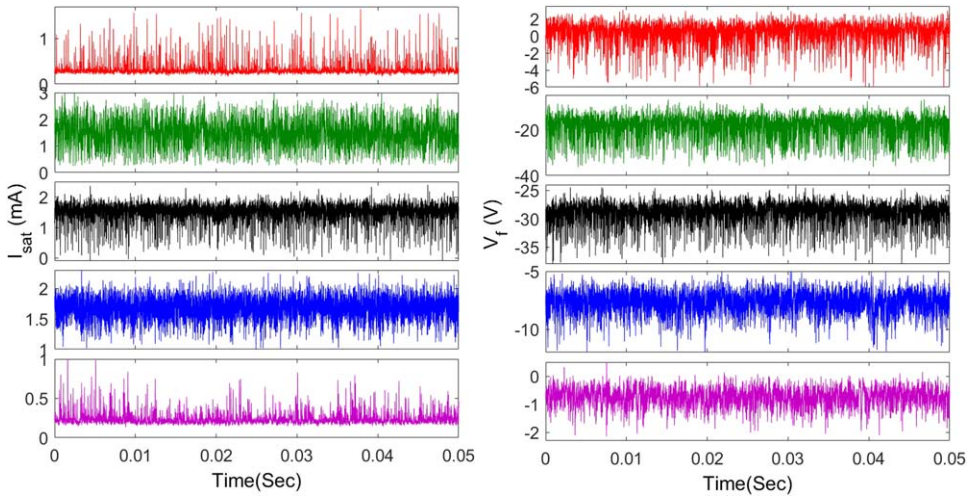

Figure 3. Raw ion saturation current, I_{sat} (left) and floating potential, V_f (right) fluctuations recorded at five different spatial locations (1 to 5 from top to bottom) in the poloidal cross-section. From top to bottom, the respective locations are: $(a, z) = (39.1,20), (12.7, -20), (-22,40), (-26, -30)$ and $(-56.4, 0)$ mm.

vertically averaged profiles to estimate the poloidal and radial velocity shears, E'_a and E'_z. It turns out that our plasma state broadly agrees with the condition $\nu'_z \sim \frac{E'_a}{B} > \nu'_a \sim \frac{E'_z}{B}$ [24]. To put our plasma regime in perspective, we have also estimated the other physical parameters associated with the current experiment in the region where electric field is maximum are as follows. The ion sound speed, $C_s = 2.19 \times 10^4$ m s^{-1}, electron plasma frequency, $f_{pe} = 2.01 \times 10^9$Hz, ion plasma frequency, $f_{pi} = 4.70 \times 10^7$Hz, electron cyclotron frequency, $f_{ce} = 1.12 \times 10^9$Hz, ion cyclotron frequency, $f_{ci} = 6.08 \times 10^5$Hz, electron-neutral collision frequency, $f_{en} = 14.4 \times 10^6$Hz, ion-neutral collision frequency, $f_{in} = 6.4 \times 10^3$Hz, electron gyro-radius, $\rho_e = 1.03 \times 10^{-4}$m and ion gyro-radius, $\rho_i = 4.4 \times 10^{-3}$m.

5. Basic statistical properties of fluctuations: moments of the distributions

Examples of typical raw I_{sat} and V_f time-series fluctuations, cropped for 5 ms duration, from five different spatial locations, (a, z), are shown in figure 3. This is a sub-set of the complete mapping of the poloidal cross-section, which was covered with evenly spaced 170 locations.

Figures 4(a), (b) show the poloidal cross-section profile of the mean of ion saturation current, $\bar{I}_{sat}$, and floating potential, $\bar{V}_f$, fluctuations reconstructed from the whole data-set. The $\bar{V}_f$ profile is more or less similar to that measured from the Langmuir characteristics as shown in figure 2(h). The $\bar{I}_{sat}$ appeared to be expanding towards the bottom of the poloidal section as in the case of time-averaged density profile, but it is characterized by a two lobes contours in low and high field side (HFS). This possibly depends on the observed deformation of the Langmuir characteristics where primary electrons coming from the filament are collected. Figures 4(c), (d) show, respectively, density, $\frac{\tilde{n}}{\bar{n}} \sim \frac{\tilde{I}_{sat,rms}}{\bar{I}_{sat}}$, and potential, $e\tilde{V}_f/kT_e$, fluctuation level, where $\tilde{I}_{sat} = I_{sat} - \bar{I}_{sat}$. Large density fluctuations with fluctuation level as high as 60% are observed in the LFS, as well as over a small region in the HFS. Whereas fluctuations are relatively small and as low as 10% in major portion of the HFS. On the other hand, potential fluctuation level exceeds 50% in the LFS, remaining small in the whole HFS. The observed level of fluctuations indicates the typical good curvature and bad curvature aspect of the HFS and LFS of toroidal devices, respectively [53].

The locations, also indicated in figure 4 maps, include both the LFS and HFS edges (1,5), as well as three locations at the boundary of the central plasma column and potential well (2–4). The I_{sat} fluctuations at location #1 and #5, are dominated by upward going events (compared to the mean), which indicate the possible characteristics of blobs. Apart from the direct visualization of the signals as reported in [6, 7], it can be verified using a number of different techniques such as higher order moments of PDF and conditional averaging in probe-based studies. In order to obtain the PDF, the time series x_i is first normalized with respect to its rms value and then a histogram is constructed by distributing its data samples of uniformly sized intervals. The probability is then determined as the ratio between the number of samples in each interval and total number of samples. In addition to the first two moments, i.e. mean ($\bar{x}$) and standard deviation (σ), the third and fourth moments, the skewness (S) and the excess kurtosis (K) are widely used. They are defined as follows:

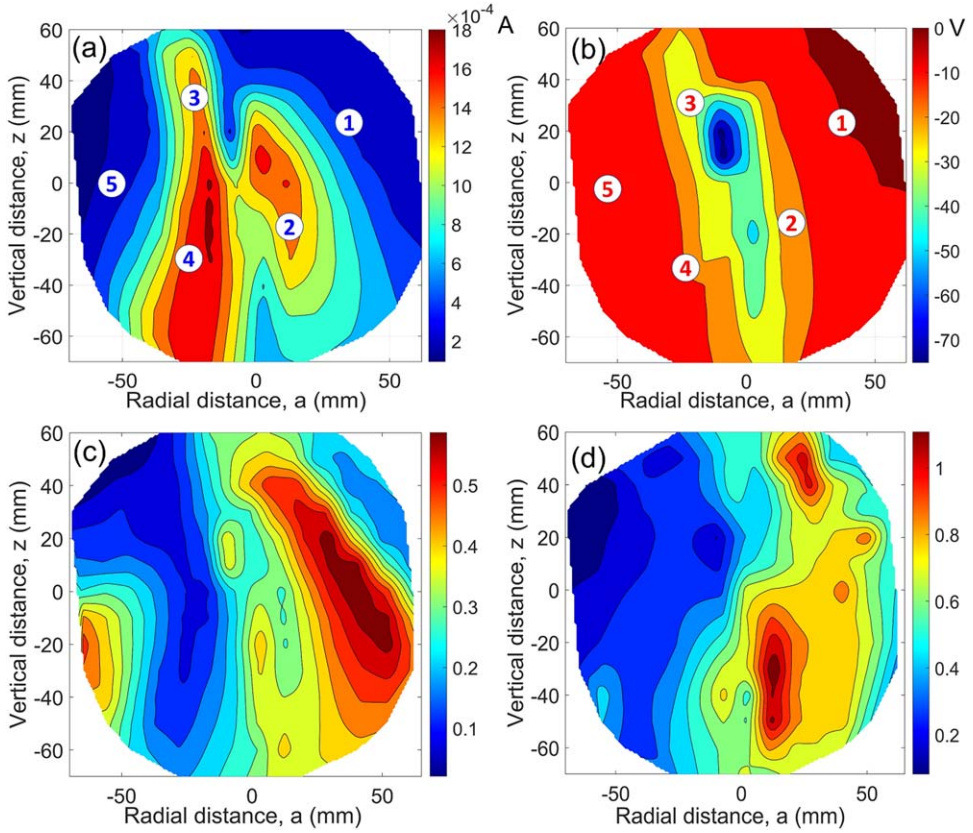

Figure 4. Time series of fluctuations measured in the poloidal cross-section: (a) Average ion saturation current, $\bar{I}_{sat}$, and (b) floating potential, $\bar{V}_f$. (c) The density and (d) floating potential fluctuation level. Five particular locations are indicated in the maps, which will be discussed in the text.

and

$$\mathrm{S} = \frac{1}{n}\frac{\sum_{i=1}^{n}(x_n - \bar{x})^3}{\sigma^3}$$

$$\mathrm{K} = \frac{1}{n}\frac{\sum_{i=1}^{n}(x_n - \bar{x})^4}{\sigma^4}.$$

For the above mentioned signals in figure 3, the measured S and K values for locations #1 and #5 are: $\mathrm{S} = 4.29, \mathrm{K} = 25.9$, and $\mathrm{S} = 2.88, \mathrm{K} = 14.9$, respectively. These values indicate the non-Gaussian nature of the distributions, dominated by a positive tail ($\mathrm{S} > 0$) of the probability distribution function (PDF), which may be interpreted as blobs. At the same time, fluctuations at #3 and #4 are composed of mostly negative events as evident from the values, $\mathrm{S} = -1.34$ and $\mathrm{K} = 6.13$, and $\mathrm{S} = -0.41, \mathrm{K} = 3.32$, respectively, which we tentatively interpret as describing holes. On the other hand, for the signal at location #2, equal numbers of positive and negative fluctuations are observed, *i.e.*, blobs and holes are formed in equal numbers, however showing a Gaussian PDF (S and K $\sim$ 3). The observed zero value of S at #2 is understood as such location corresponding to the region of blob birth [22]. At the same time, strong negative intermittent features are observed for V_f fluctuations nearly at all locations.

To identify the spatial extent of blob and hole region, 2D profiles of S and K are obtained from $\tilde{I}_{sat}$ fluctuations as shown in figures 5(a), (b), where the former is overlapped with $\tilde{I}_{sat}$ level of fluctuation. Three regions can be identified in figure 5. A poloidally elongated region in the LFS having a length of $\sim$6 cm and width of $\sim$2 cm with moments as high as $\mathrm{S} = 5.3$ and $\mathrm{K} = 47$, respectively, represents the region of maximum probability of occurrence for blob events. This region lies parallel but outside the region of maximum electric field (see figure 2(i)), but also at the outside edge of maximum fluctuation amplitude region, as it can be seen from the overlapped contour. Secondly, a vertically elongated region with $\mathrm{S} < 0$, indicated using red dashed contour, represents the hole zone. Third, lying between the other two regions, a zone characterized by $\mathrm{S} \approx 0$, which also corresponds roughly to location where large velocity shears happen.

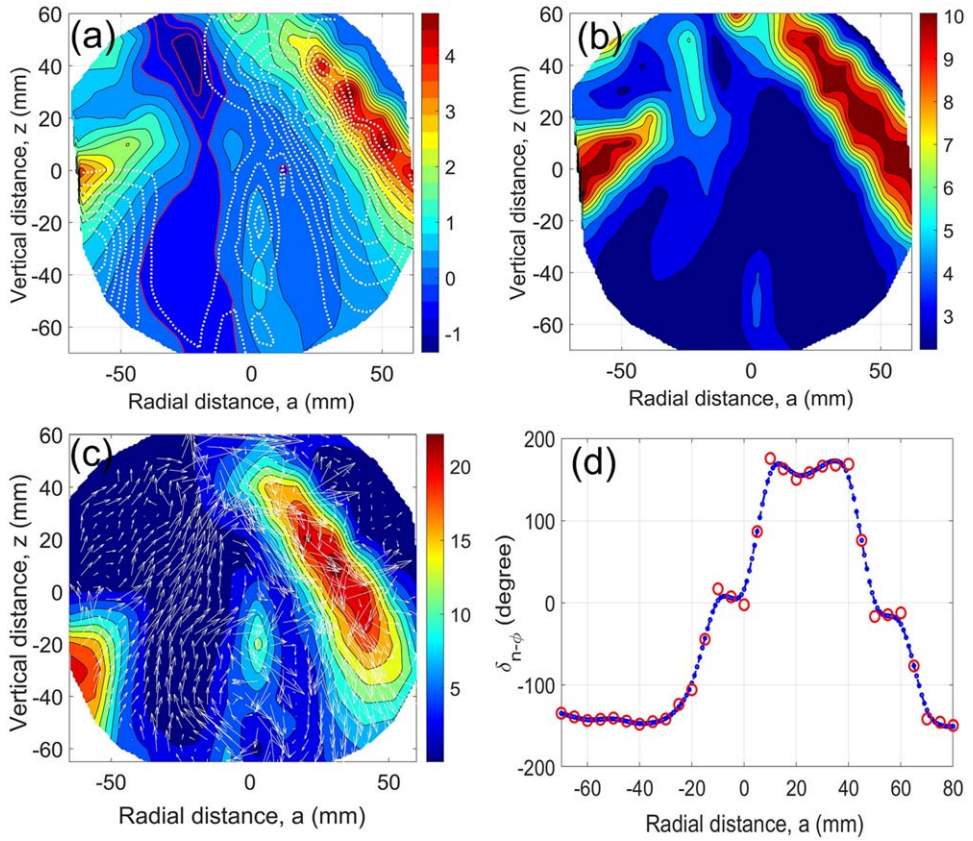

Figure 5. Maps of the poloidal cross-section profiles of (a) Skewness (S) and (b) Kurtosis (K) of I_{sat} fluctuations. Figure 5(a) is overlapped with corresponding density fluctuation level (dotted lines). To get a clear topological view, K distribution in the poloidal section is limited to K = 10. (c) Distribution of spectral power for the dominant frequency component. (d) The cross phase between density and potential fluctuations along the diagonal described in the system schematic.

Further, an attempt was taken to identify the dominant modes. FFTs were calculated for each time series. They generally show a low-frequency peak, in (10−20) kHz range, slightly changing at different locations. Figure 5(c), shows the spatial distribution of the peak spectral power in the 2D poloidal cross-section estimated from the autopower spectrum of the normalized signal. Since it almost coincides with the regions where large fluctuation levels are observed, we could conclude that these correspond to zones dominated by an almost single mode with frequency component of ∼13 kHz. We measured simultaneously ion saturation and floating potential fluctuations along the inclined line shown in figure 1. We calculated the cross-phase angle for the peak frequency, $\Theta = \mathrm{Ang}(\tilde{I}_{sat}, \tilde{V}_f)$, which is displayed in figure 5(d). It could be noticed that $\Theta > 90^0$ in the LFS region where spectral power peaks. This indicates that the dominant mode has an interchange nature [39, 54, 55]. Additional studies suggest that the observed $\tilde{I}_{sat}$ fluctuations exhibit a universal parabolic characteristic between S and K for intermittent turbulent fluctuations [7, 56–59]. Figure 6 shows S versus K of I_{sat} signals estimated from nearly 170 locations over the complete poloidal cross-section as a function of relative amplitude of fluctuations. A unique parabolic feature is observed in the plot which can be fitted with a second-order quadratic polynomial, $K = 1.4\,S^2 + 0.14\,S + 2.89$, indicating the significance of fluctuation while making a comparison with that of SOL of tokamak.

6. Conditional sampling and spatio-temporal evolution of turbulent structures

Although previous section provides information about the region where blobs and holes exist, but the generation mechanism, spatio-temporal evolution, propagation etc are unclear. In this section, conditional averaging analysis of $\tilde{I}_{sat}$ and $\tilde{V}_f$ fluctuations are used to reconstruct the snapshot of 2D structures at different time to investigate these aspects. Additional details of conditional averaging analysis technique can be found elsewhere [49, 60, 61]. This technique extracts coherent part of the fluctuation from asynchronous measurements taken from different spatial locations. It involves simultaneous measurement of time series signals from a fixed (reference) probe and a scan probe. In our data, the latter one scans the whole poloidal plane under investigation. Then an averaging is performed based on the event selection and the threshold set at the

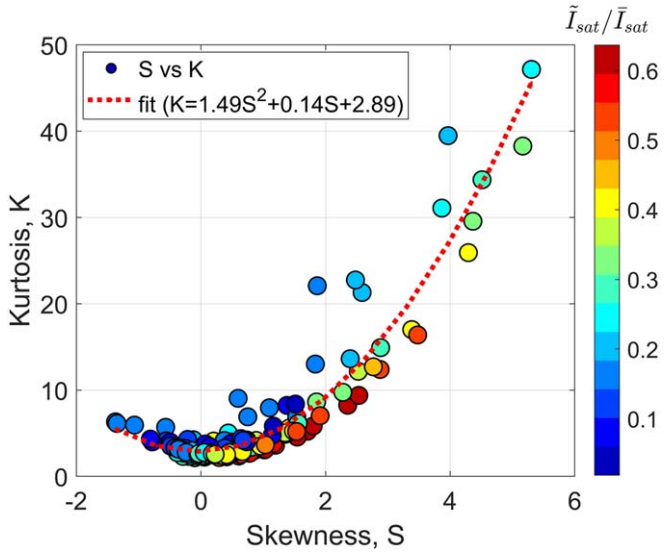

Figure 6. Skewness of nearly 170 I_{sat} signals measured from the complete poloidal profile plotted against respective kurtosis value as a function of relative amplitude of fluctuation. A unique statistical relation between both is drawn using a second order polynomial.

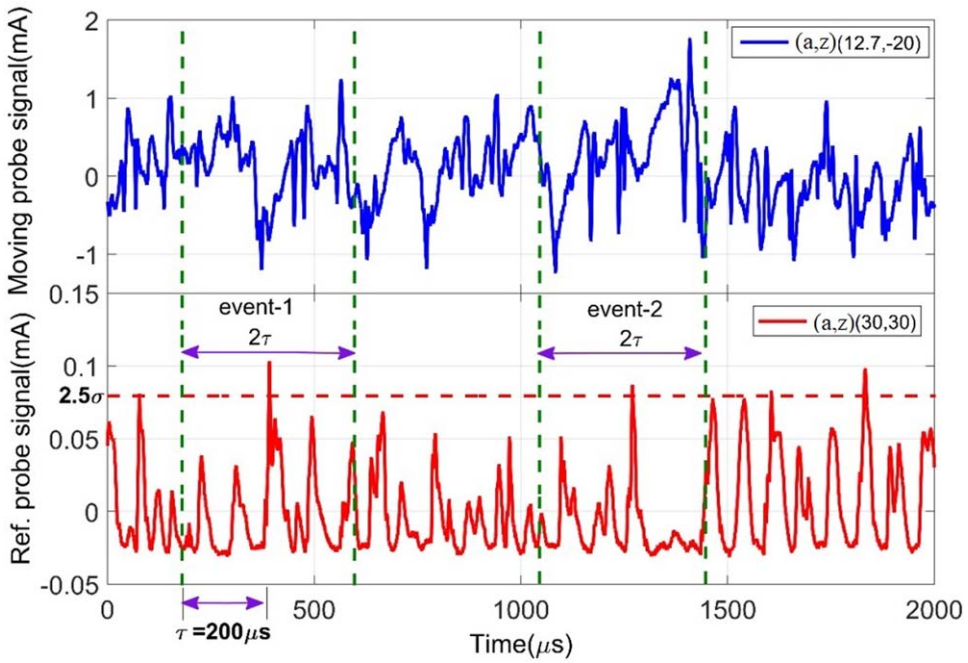

Figure 7. Illustration of the procedure for identifying an event and obtaining cross conditional average of a time series is shown. Top traces shows the time series of a moving probe signal and bottom trace shows that of a ref. probe signal obtained simultaneously. Events are idenfified when the amplitude exceed selected threshold of 2.5 σ. Two pairs of vertical green line indicate the the time window of width $2\tau = 400$ μs selected around two event.

reference probe. Similar routine for time series from whole poloidal cross-section helps in reconstructing the 2D structure for different time delay.

Illustration of one such averaging performed at one location in the poloidal cross section for the $\tilde{I}_{sat}$ signal is shown in figure 7. The lower panel shows a 2000 μs segment of $\tilde{I}_{sat}$ reference probe time series from a fixed location of $(a\,, z) = (25, 15)$ mm and the upper panel shows the same from the scan probe when it was located at $(a\,, z) = (12.7, -20)$ mm. For a threshold condition of 2.5σ set at the reference probe signal (horizontal dashed line), analysis detects two events (two blobs since the probe triggered for upward going events at $+2.5\sigma$), marked as event-1 & event-2 as shown in figure where σ is the standard deviation of the signal [34]. The threshold values were chosen as a compromise between having enough events in the reference probe time series (here never less and generally about 1000) and enough large fluctuation amplitudes. We also checked that increasing the

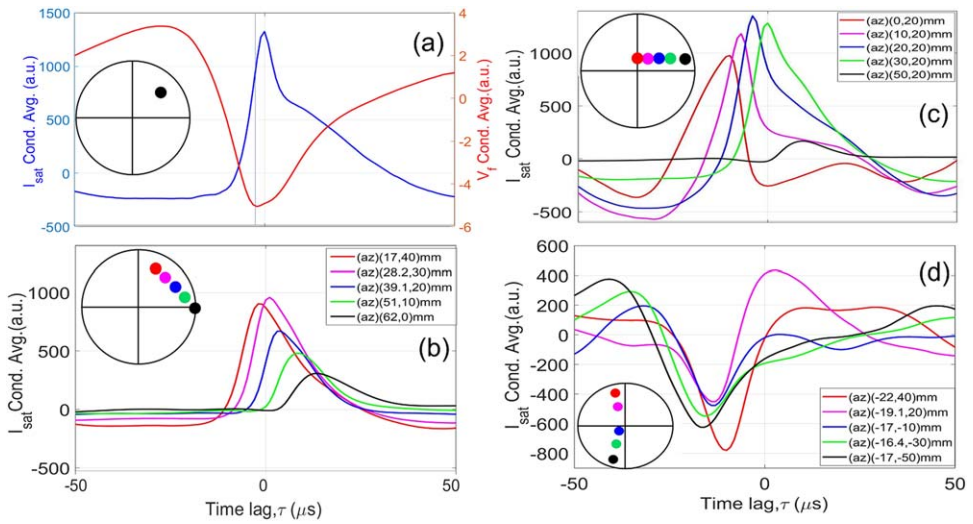

Figure 8. (a) The conditional averaged $\tilde{I}_{sat}$ and $\tilde{V}_f$ waveform at the reference probe, *i.e.,* autoconditional average. Cross conditionally averaged waveform, C ($\tilde{I}_{ref}$*$\tilde{I}_{scan}$), in: (b) The region where skewness is maximum; (c) along a horizontal line; (d) the hole region. The location of data collected are shown in the insets.

threshold will not affect the observed temporal evolution of the intermittent structures. A time window of $\tau = 200$ μs is then selected around such events. This time interval length is larger than the typical autocorrelation time of the corresponding fluctuations. The same procedure is performed over the whole length of the time series to identify such events. In this study, the number of blob events detected was approximately between 1100 and 1400 for a signal of one second duration at different poloidal location. The corresponding scan probe time series data is then averaged to eliminate the contribution of fluctuations not correlated with the event selected at the reference position gives the conditionally averaged (CA) density fluctuation or blob pulse at that particular location. Similarly, for the detection of hole events a threshold of $-1.5\,\sigma$ is used at the reference probe.

Before moving to the 2D reconstruction, figure 8 provides 1D waveform (time history) of conditionally averaged $\tilde{I}_{sat}$ and $\tilde{V}_f$ fluctuation from few selected areas of interest as it is useful to extract some useful information such as pulse shape, evolution and estimation of propagation velocity.

Figure 8(a) shows the time waveforms of $\tilde{I}_{sat}$ and $\tilde{V}_f$ derived by performing conditional averaging for blob events of the signal at the reference probe with itself (autoconditional average, ACA [20]), *i.e.,* C($\tilde{I}_{ref}$*$\tilde{I}_{ref}$) to be compared with the floating potential signal, C($\tilde{I}_{ref}$*$\tilde{V}_f$), obtained when the scan probe is at the reference probe location. ACA of $\tilde{I}_{sat}$ signal yields an asymmetric large amplitude positive pulse with its maximum at 0 μs. This blob structure is characterized by a steep rise at ~14 μs and a slow decay up to 56 μs, effectively giving a time scale width of ~70 μs. This mere positive pulse over a constant background density indicates the passage of an isolated blob strucutre across this location. On the other hand, the $\tilde{V}_f$ waveform has both a minimum and a maximum values. The minimum value with an amplitude of ~−5 V exists at the same location as $\tilde{I}_{sat}$ maximum, and the maximum value occurs to the left of it with an amplitude of ~4 V.This implies that within the given time range of [−50,50] μs, the potential structure changes from positive to negative at the reference probe location. The remaining plots show the cross conditional averaging (CA) between reference probe and scan probe, C($\tilde{I}_{ref}$*$\tilde{I}_{scan}$), and the scan probe location is shown in the insets of figure 8.

An effort is taken to examine the time waveform in the blob region or where skewness is high as shown in figure 8(b). The maps are characterized by a pulse shape having a steep leading edge and a trailing wake with flat base. This pure monopole distribution of high-density structure over a low-density background clearly indicates the passage of blobs along this region. The steep leading edge and trailing wake are attributed to the sheared flow pattern produced as the blob interacts with the background density. Note that the leading edge is to the left and blob structure peaks at (−2, 1, 4, 8, 14) μs for pulses shown from left to right, implying outward clockwise motion with respect to the reference probe pulse (0 μs). The time scale width and amplitude decreased as it approaches the edge indicating the decay of the blob structure during its motion as well as with progress in time. The poloidal velocity of the blob structure in this region can be estimated by measuring the time delay of propagation and is given by ~3.75 km s^{-1}. This value is of the order of background $\nu_{E\times B}$ measured from the equilibrium profile. In a similar manner, waveforms generated in the horizontal plane along $z = 20$ mm are shown in figure 8(c). Unlike the previous case, it shows that the positive fluctuation is anticipated by a significant negative part, meaning that the structure here is not a pure blob as seen in the previous case, but it consists by

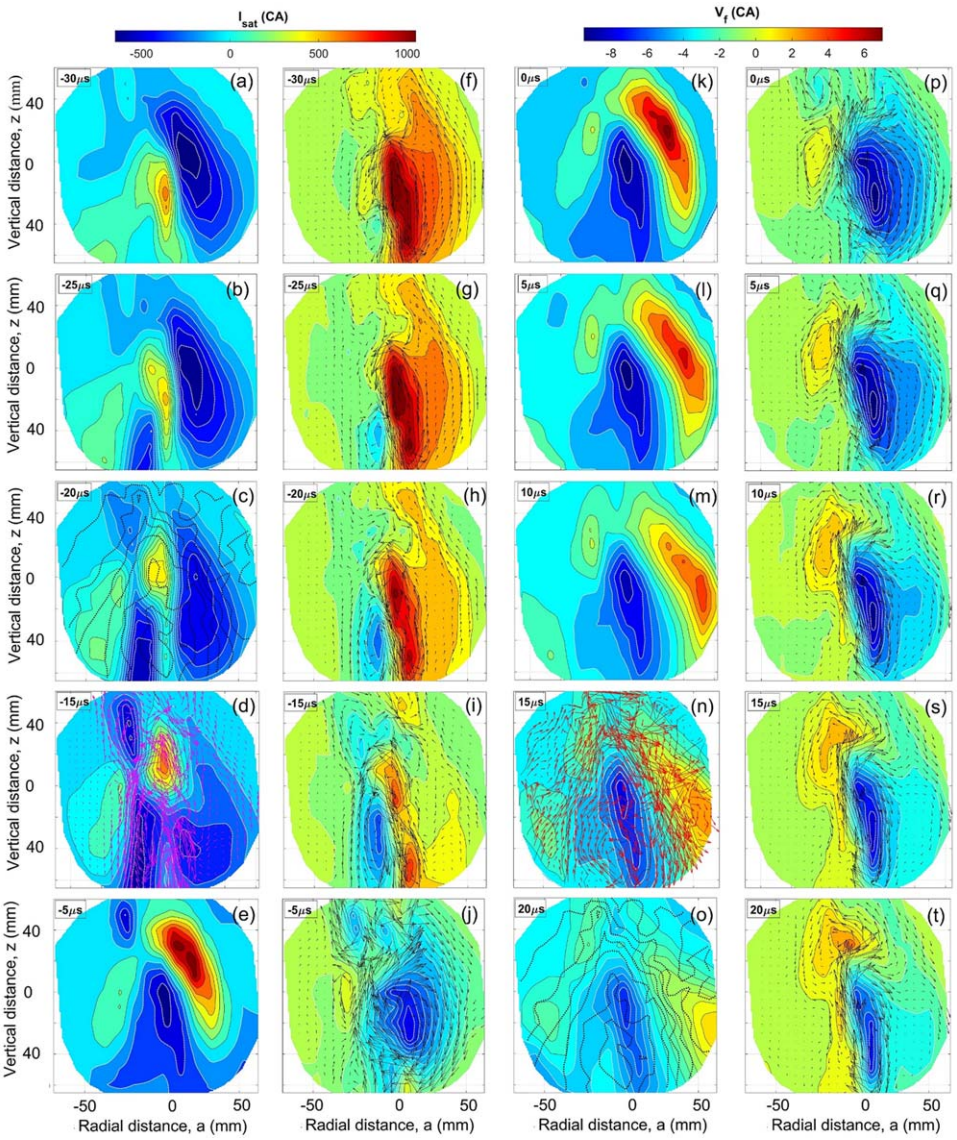

Figure 9. Spatio-temporal evolution of density (1st and 3rd columns) and potential structures (2nd and 4th columns), for time delay between -30 μs and 20 μs, generated for a threshold of $+2.5\,\sigma$. Time averaged potential contour is overlapped in (c) and (o) and that of $\boldsymbol{E} \times \boldsymbol{B}$ flow field is shown in (n). Fluctuating $\boldsymbol{E} \times \boldsymbol{B}$ flow field is overlapped in every snapshot of potential structure and also in (d).

dipolar structure moving across the selected location. Further, waveform in the high-density region is shown in figure 8(d), indicating the waveform is dominated by downward going pulse, a signature of a, mostly isolated, hole. Since the plasma column is a rotating one, drawing a conclusion on the 2D structure and its trajectory can be obtained by looking at the conditional averaged signal of the whole poloidal section, with time delay between -30 μs and 20 μs. This is the time window by which CA has the highest statistical confidence.

6.1. Blob structures

Snapshots of spatio-temporal evolution of density $C(\tilde{I}_{ref}, \tilde{I}_{scan})$ (1st and 3rd columns) and potential $C(\tilde{I}_{ref}, \tilde{V}_{scan})$ (2nd and 4th columns) structures in the poloidal section between time delay -30 μs and 20 μs is shown in figure 9. Positive structures are highlighted using solid black contour and negative structures are isolated with dashed white contour. The location of the reference probe is marked in the first picture, figure 9(a). A general trend observed in the density structure is that both positive and negative structure exist simultaneously in space and are tightly coupled and rotating in the clockwise direction. Figure 9(a), depicts that at -30 μs, a negative structure occupies most of the LFS while a positive structure exists in the HFS with its maximum amplitude region is in the shear layer. As the time progresses, the structure rotates clockwise but the radially elongated part of the positive structure breaks into two, figures 9(a)–(e), by the differential stretching exerted by the background instantaneous $\boldsymbol{E} \times \boldsymbol{B}$ field which is shown using overlapped flow field in figure 9(d). During this process, different parts of the structure either move in opposite direction or move with relative velocity causing the leading part of the structure detach

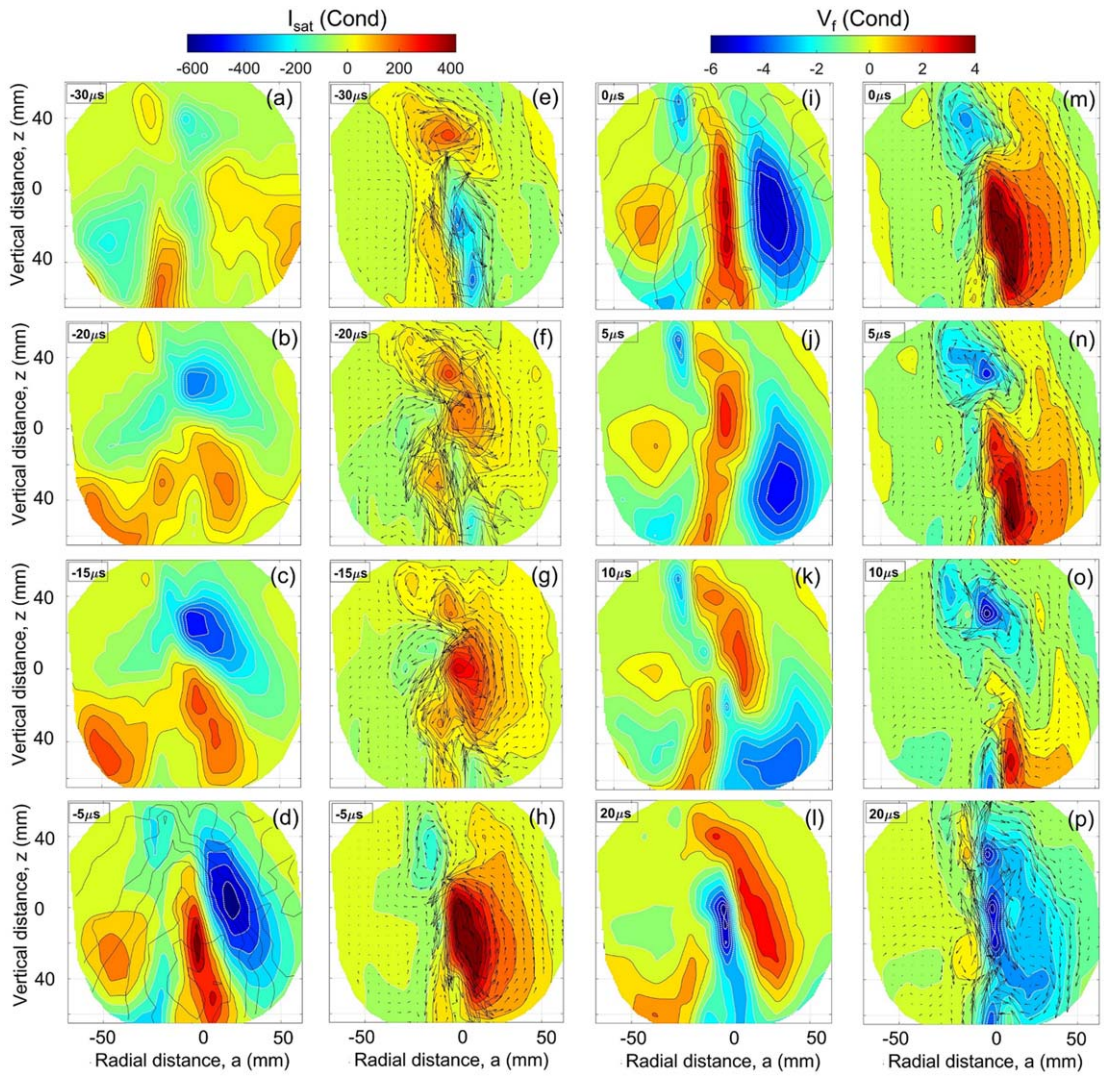

Figure 10. Spatio-temporal evolution of density (1st and 3rd columns) and potential strucutres (2nd and 4th columns) for time dealy between -30 μs and 20 μs, generated for a threshold of -1.5 σ. Time averaged potential contour is overlapped in (d) and (i), and fluctuating $\boldsymbol{E} \times \boldsymbol{B}$ flow field is overlapped in every snapshot of potential structure.

from the trailing part. The leading part of the structure in the shear layer region emerges out as an isolated blob structure. At the same time, it should be noticed that during this process, the negative structure is mostly propagating inside or along the contour corresponding to $V_P = 0$ as shown in figure 9(c) (contour is overlapped). The isolated blob is then convected within the LFS outside of the $V_P = 0$ contour.

As shown in figures 9(k)–(o), the structure undergoes an elongation, its amplitude decays and it is ultimately ejected to the limiter at 20 μs. Blob structure having maximum amplitude is observed at 0 μs where its length is nearly equal to minor radius of the system and having a width of $\sim$2 cm. The potential structures given at every time delay depicts a modification of the background $\boldsymbol{E} \times \boldsymbol{B}$ velocity field that is in broad agreement with the observed density structure propagation. Unlike the density structure, potential structure is mostly dominated by monopole structure in space. For example, at -30 μs, the potential structure consists of a positive structure, while negative structure is nearly absent. This has a maximum potential of $\sim+7$ V at the center, whose corresponding fluctuating $\boldsymbol{E} \times \boldsymbol{B}$ velocity field dictates a rotation in a counter clockwise direction, for negative density structure in the LFS as seen in figure 8(a). Similarly it happens at 0 μs, with a potential structure which is dominated by a negative structure with a potential minimum of ~-9.5 V at the center and the derived fluctuating $E \times B$ field is in the clockwise direction as displayed in figure 9(p).

6.2. Hole structures

In a similar way, hole dynamics is studied by triggering the events at the reference probe by setting a threshold of -1.5σ In figure 10, the 1st and 3rd columns represent the density structures, and 2nd and 4th denote the

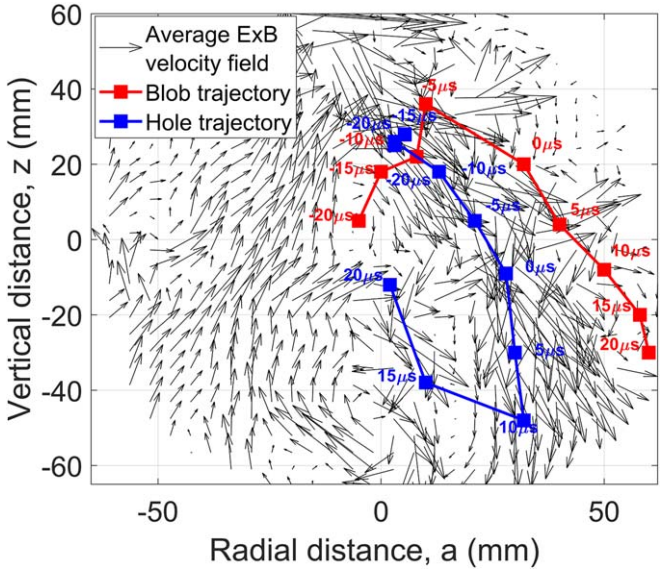

Figure 11. Trajectories of blob (red square) and hole (blue square) are shown over the time averaged $E \times B$ field.

potential structure. In the case of hole events, initially, as in figure 10(a), there is no density structure correlated with the reference signal in the poloidal cross-section. As the time progresses, the hole structure gains in amplitude and begins to expand in the LFS, figures 10(b)–(d), while the positive structure, being a narrow one, gets elongated in the shear layer. Unlike the case of blob structure observed in the previous section at 20 μs, the hole structure is not getting lost to the limiter but moves along the $V_p = 0$ potential contour, figures 10(d)–(k), and driven back to the main plasma as shown in figure 10(l). It should be noted that the potential structure and derived fluctuating $E \times B$ field modify the density structure propagation in the opposite way respect to the case of blobs, in broad agreement with the different evolution reported.

Trajectories of both blob and hole are compared in figure 11, and shown over the time-averaged $\boldsymbol{E \times B}$ drift field. Data show that at -10 μs both blob (positive structure in figure 9) and hole (negative structure in figure 10) exist nearly at the same location in the poloidal cross section. But as the time progresses, the hole structure moves faster along the maximum radial electric field region, while the blob structure is propagating outside this region. At 5 μs, both are spatially separated by nearly ~40 mm and 20 μs, the blob reaches the edge of the plasma while the hole structure is driven back to the main plasma.

6.3. Cross-correlation analysis

It is known that statistical uncertainties can largely affect identification of large-scale structures when analysis is performed using the two-point correlation method [25]. Since we have seen large-amplitude fluctuations in the system, the cross-correlation method can still be used as a useful tool to confirm the findings of the conditional averaging method. Cross-correlation, C_r between simultaneously acquired scan probe signal and reference probe signal is shown in figure 12 for density and potential fluctuations, *i.e.* $C(\tilde{I}_{ref}, \tilde{I}_{scan})$ and $\boldsymbol{C_r}(\tilde{\boldsymbol{I}}_{\boldsymbol{ref}}, \tilde{\boldsymbol{V}}_{\boldsymbol{scan}})$. The first row represents $\boldsymbol{C_r}(\tilde{\boldsymbol{I}}_{\boldsymbol{ref}}, \tilde{\boldsymbol{I}}_{\boldsymbol{scan}})$ and the second row denotes $\boldsymbol{C_r}(\tilde{\boldsymbol{I}}_{\boldsymbol{ref}}, \tilde{\boldsymbol{V}}_{\boldsymbol{scan}})$, for time delays $(-30, 0, 20)$ μs, respectively. In figure 12(a), a negative correlation, with $\boldsymbol{C_r}(\tilde{\boldsymbol{I}}_{\boldsymbol{ref}}, \tilde{\boldsymbol{I}}_{\boldsymbol{scan}}) < -0.6$, and a positive correlation of ~0.5 are observed in the LFS and near the center respectively. At 0 μs delay, correlations as high as 0.8 and as low as -0.7 are observed simultaneously. With increase in time delay, the positive correlation drops, as the structure propagates towards the limiter. In general, the cross-correlation plots agree with the conditional averaging observations but they slightly overestimate the size and lifetime of the structures. This was observed comparing the structure at 10 μs and 20 μs in the cross-correlation with those reconstructed by the conditional averaging analysis. The length of the structure is larger than the system minor radius and width is larger than ~2 cm. Further, the density structures are mostly localized isolated structures and they have a higher correlation along the poloidal direction than along the radial direction, with typical correlation times of 10–20 μs. Likewise, $\boldsymbol{C_r}(\tilde{\boldsymbol{I}}_{\boldsymbol{ref}}, \tilde{\boldsymbol{V}}_{\boldsymbol{scan}})$ yields nearly a similar structure as observed in conditional sampling. Unlike $\boldsymbol{C_r}(\tilde{\boldsymbol{I}}_{\boldsymbol{ref}}, \tilde{\boldsymbol{I}}_{\boldsymbol{scan}})$, simultaneous existence of both maximum and minimum is not observed for $\boldsymbol{C_r}(\tilde{\boldsymbol{I}}_{\boldsymbol{ref}}, \tilde{\boldsymbol{V}}_{\boldsymbol{scan}})$ for a given time delay, indicating that they have either a single vortex nature, or that floating potential fluctuations have more extended nature rather than just being local ones.

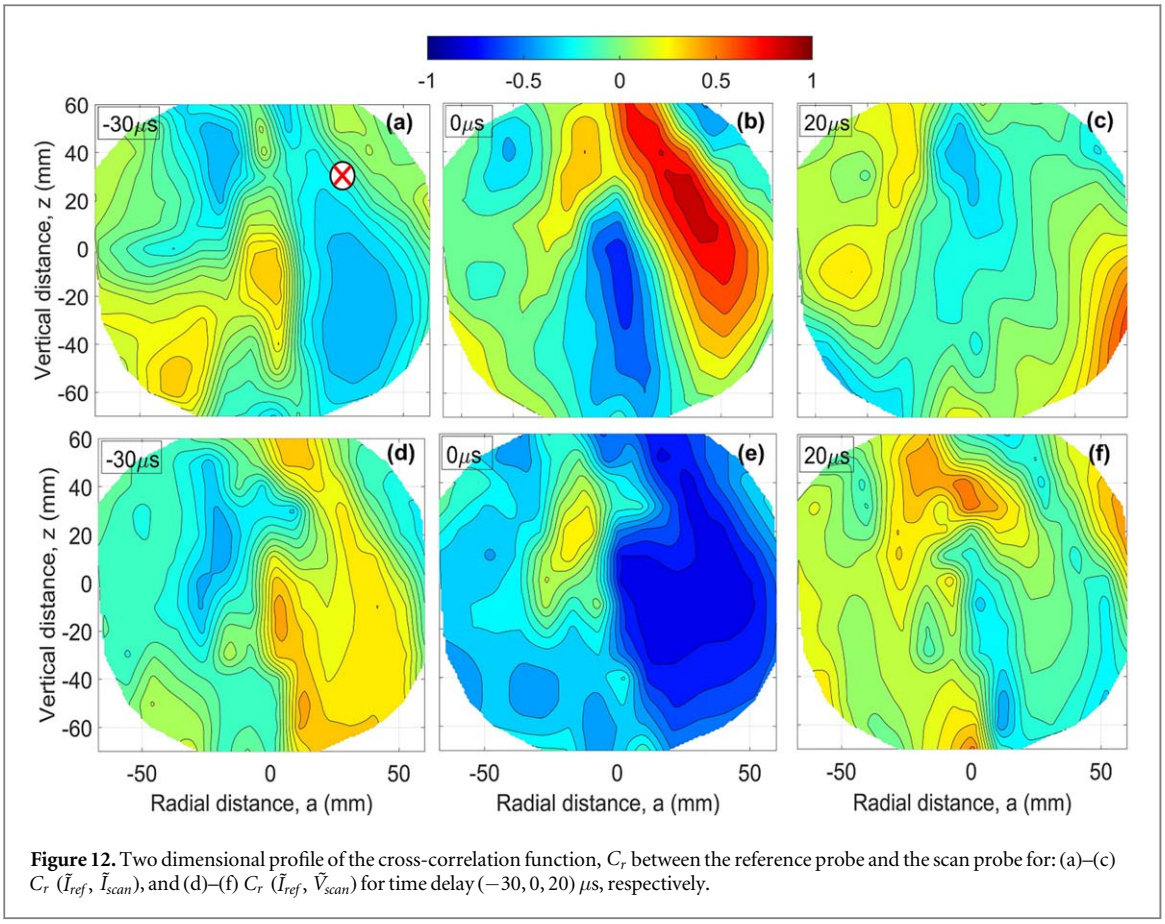

Figure 12. Two dimensional profile of the cross-correlation function, C_r between the reference probe and the scan probe for: (a)–(c) C_r $(\tilde{I}_{ref}, \tilde{I}_{scan})$, and (d)–(f) C_r $(\tilde{I}_{ref}, \tilde{V}_{scan})$ for time delay $(-30, 0, 20)$ μs, respectively.

7. Summary and conclusions

In summary, experiments are performed in the simple magnetized toroidal plasma device THORELLO to investigate the dynamics of large-scale coherent structures in density and potential fluctuations in an open field line configuration. Open helical magnetic field line configuration in the system is realized by superposing a vertical field to the purely toroidal field. In the reported experiments the opened up field lines are then characterized by a connection length of $\boldsymbol{L_c \approx 2333}$ cm and pitch ratio $\boldsymbol{r_B \approx 7.5 \times 10^{-3}}$. A quasi-stationary equilibrium is established by the helical field results in vertically elongated equilibrium plasma profiles with significant gradients in density, potential and electron temperature. The equilibrium electric field arising from the negative biasing of the source makes the hydrogen plasma rotating asymetrically with $\boldsymbol{E \times B}$ poloidal velocity shear in the system in the direction of electron diamagnetic drift. This plasma configuration was not experimentally investigated yet. Large amplitude fluctuations are observed in the low field side. Statistical analysis of ion saturation current fluctuations indicated the existence of strong localized intermittent fluctuations in the system. A low-density region in the LFS is characterized by upward going positive fluctuations (compared with the mean) or density enhanced structures termed as blob filaments. Downward going events or holes are detected in the high-density core plasma region. An intermediate region, separating both holes and blob region is identified with fluctuations having Gaussian statistics considered as blob birth zone. Further, detailed conditional sampling analysis is performed to investigate the spatio-temporal evolution of density and potential structures. Conditionally averaged density fluctuations are characterized by a monopole blob pulse having a steep leading edge and a trailing wake in the strong positive intermittent layer. Analysis shows density structures propagate in a poloidal trajectory in the clockwise direction with background $\boldsymbol{E \times B}$ velocity. A differential stretching arising from the background fluctuating field, breaks the poloidally elongated structure in the vicinity of the shear layer. The structure breaks off from the elongated structure and it emerges as an isolated blob which then propagates into the low field side by the background $\boldsymbol{E \times B}$ drift. These structures have long spatial correlation along the plasma flow direction in the low field side with approximate length of the order of system minor radius. Advection of blobs to the walls is observed when they propagate beyond the last closed equipotential contours, which is accompanied by simultaneous inward propagation of holes which was always found to move along or inside the same contour. The derived fluctuating potential structure supports the blob and hole propagation since the direction of fluctuating $\boldsymbol{E \times B}$ velocity field within the structure is clockwise and

counter-clockwise for negative and positive structures, respectively. Cross-correlation analysis is in broad agreement with conditionally averaged maps.

Acknowledgments

The data that support the findings of this study are available upon reasonable request from the authors.

Data availability statement

The data that support the findings of this study are available upon reasonable request from the authors.

ORCID iDs

Prince Alex https://orcid.org/0000-0001-8191-4573
Ruggero Barni https://orcid.org/0000-0001-8910-5156
Hector Eduardo Roman https://orcid.org/0000-0003-3183-9258
Claudia Riccardi https://orcid.org/0000-0002-3983-5414

References

[1] Zweben S J, Boedo J A, Grulke O, Hidalgo C, LaBombard B, Maqueda R J, Scarin P and Terry J L 2007 *Plasma Phys. Controlled Fusion* **49** S1
[2] Boedo J A *et al* 2003 *Phys. Plasmas* **10** 1670
[3] Endler M 1999 *J. Nucl. Mater.* **266–269** 84
[4] Luxon J L 2002 *Nucl. Fusion* **42** 614
[5] Happel T, Greiner F, Mahdizadeh N, Nold B, Ramisch M and Stroth U 2009 *Phys. Rev. Lett.* **102** 255001
[6] Xu G S *et al* 2009 JET EFDA Contributors *Nucl. Fusion* **49** 092002
[7] Nold B, Conway G D, Happel T, Müller H W, Ramisch M, Rohde V, Stroth U and ASDEX-U Team 2010 *Plasma Phys.Controlled Fusion* **52** 065005
[8] Myra J R, D'Ippolito D A and Russell D A 2015 *Phys. Plasmas* **22** 042516
[9] Sanchez R, van Milligen B, Newman D and Carreras B 2003 *Phys. Rev.Lett.* **90** 185005
[10] Manz P, Ribeiro T T, Scott B D, Birkenmeier G, Carralero D, Fuchert G, Müller S H, Müller H W, Stroth U and Wolfrum E 2015 *Phys. Plasmas* **22** 022308
[11] Russell D *et al* 2015 *Phys. Plasmas* **22** 092311
[12] Zweben J, Myra J R, Davis W M, D'Ippolito D A, Gray T K, Kaye S M, LeBlanc B P, Maqueda R J, Russell D A, Stotler D P and NSTX-U Team 2016 *Plasma Phys. Control. Fusion* **58** 044007
[13] Garcia O E, Bian N H and Fundamenski W 2006 *Phys. Plasmas* **13** 082309
[14] Bisai N, Das A, Deshpande S, Jha R, Kaw P, Sen A and Singh R 2005 *Phys. Plasmas* **12** 102515
[15] Nielsen A H, Pecseli H L and Rasmussen J J 1996 *Phys. Plasmas* **3** 1530
[16] Brochard F, Windisch T, Grulke O and Klinger T 2006 *Phys. Plasmas* **13** 122305
[17] Pierre T, Escarguel A, Guyomarc'h D, Barni R and Ricardi C 2004 *Phys. Rev. Lett.* **92** 065004
[18] Barni R, Riccardi C, Pierre T, Leclert G, Escarguel A, Guyomarc'h D and Quotb K 2005 *New J. Phys.* **7** 225
[19] Carter T A 2006 *Phys. Plasmas* **13** 10701
[20] Antar G Y 2003 *Phys. Plasmas* **10** 3629
[21] Magni S, Riccardi C and Roman H E 2004 *Phys. Plasmas* **11** 4564
[22] D'Ippolito D A, Myra J R and Zweben S J 2011 *Phys. Plasmas* **18** 060501
[23] Müller S H, Theiler C, Fasoli A, Furno I, Labit B, Tynan G R, Xu M, Yan Z and Yu J H 2009 *Plasma Phys. Controlled Fusion* **51** 055020
[24] Bisai N, Banerjee S and Sen A 2019 *Phys. Plasmas* **26** 020701
[25] Grulke O, Greiner F, Klinger T and Piel A 2001 *Plasma Phys. Control. Fusion* **43** 525
[26] Kaur R, Singh A K, Singh R, Sarada S A and Mattoo S K 2011 *Phys. Plasmas* **18** 012109
[27] Oynes F J, Olsen O M, Pécseli H L, Fredriksen Å and Rypdal K 1998 *Phys. Rev.* E **57** 2242
[28] Rypdal K, Gronvoll E, Oynes F, Fredriksen A, Armstrong R J and Trulsen J 1994 *Plasma Phys. Controlled Fusion* **36** 1099
[29] Fredriksen Å, Riccardi C and Cartegni L 2003 *Rev. Sci. Instrum.* **74** 1588
[30] Trasarti-Battistoni R, Draghi D and Riccardi C 2002 *Phys. Plasmas* **9** 3369
[31] Riccardi C and Fredriksen Å 2001 *Phys. Plasmas* **8** 199
[32] Fredriksen A, Riccardi C, Cartegni L, Trasarti-Battistoni R and Roman H E 2003 *Phys. Plasmas* **10** 4335
[33] Riccardi C, Longoni G, Chiodini G and Fontanesi M 2001 *Rev. Sci. Instrum.* **72** 461
[34] Barni R and Riccardi C 2009 *Plasma Phys. Controlled Fusion* **51** 085010
[35] Riccardi C, Xuantong D, Salierno M, Gamberale L and Fontanesi M 1997 *Phys. Plasmas* **4** 3749
[36] Barni R, Alex P and Riccardi C 2021 *Rev. Sci. Instrum.* **92** 023512
[37] Alex P, Barni R, Ghorbanpour E and Riccardi C 2021 *Rev. Sci. Instruments* **92** 043533
[38] Fasoli A, Labit B, McGrath M, Müller S H, Plyushchev G, Podestà M and Poli F M 2006 *Phys. Plasmas* **13** 055902
[39] Poli F M, Ricci P, Fasoli A and Podestà M 2008 *Phys. Plasmas* **15** 032104
[40] Greiner F, Block D and Piel A 2004 *Contrib. Plasma Phys.* **44** 335–46
[41] Fredriksen A, Riccardi C, Cartegni L and Pecseli H L 2003 *Plasma Phys. Controlled Fusion* **45** 721
[42] Rypdal K and Ratynskaia S 2005 *Phys. Rev. Lett.* **94** 225002
[43] Gentle K W and He H 2008 *Plasma Sci. Technol.* **10** 284

[44] Li B, Rogers B N, Ricci P and Gentle K W 2009 *Phys. Plasmas* **16** 082510
[45] Müller S H, Fasoli A, Labit B, McGrath M, Podestà M and Poli F M 2004 *Phys. Rev. Lett.* **93** 165003
[46] Furno B *et al* 2008 *Phys. Rev. Lett.* **100** 055004
[47] Theiler C, Diallo A, Fasoli A, Furno I, Labit B, Podestà M, Poli F M and Ricci P 2008 *Phys. Plasmas* **15** 042303
[48] Barni R, Caldirola S, Fattorini L and Riccardi C 2017 *Phys. Plasmas* **24** 032306
[49] Pécseli H L and Trulsen J 1989 *Phys. Fluids* B **1** 1616
[50] Ricci P and Rogers B N 2010 *Phys. Rev. Lett.* **104** 145001
[51] Kumar U, Thatipamula S G, Ganesh G, Saxena Y C and Raju D 2016 *Phys. Plasmas* **23** 102301
[52] Grulke O and Klinger T 2002 *New J. Phys.* **4** 67
[53] Kikuchi M, Lackner K and Tran M Q 2012 *Fusion Physics* (Wien: IAEA)
[54] Jassby D L Short S C and Shah N *Phys. Fluids* **15** 1590
[55] Desjardins T R and Gilmore M 2016 *Phys. Plasmas* **23** 055710
[56] Labit B, Furno I, Fasoli A, Diallo A, Muller S H, Plyushchev G, Podesta M and Poli F M 2007 *Phys. Rev. Lett.* **98** 255002
[57] Cristelli M, Zaccaria A and Pietronero L 2012 *Phys. Rev.* E **85** 066108
[58] Guszejnov D, Lazanyi N, Bencze A and Zoletnik S 2013 *Phys. Plasmas* **20** 112305
[59] Labit B, Theiler C, Fasoli A, Furno I and Ricci P 2011 *Phys. Plasmas* **18** 032308
[60] Fattorini L, Fredriksen Å, Pécseli H L, Riccardi C and Trulsen J K 2012 *Plasma Phys. Control. Fusion* **54** 085017
[61] Roman H E, Lambin P, Malaise E P and Robson T 2007 *Rev. Sci. Instruments* **78** 123502